Correlations of nanoscale film morphologies and topological confinement of three-arm cage block copolymers†

Brian J. Ree,[a] Yusuke Satoh,[b] Takuya Isono,[a] and Toshifumi Satoh[a,*]

[a]Faculty of Engineering, Hokkaido University, Sapporo 060-8628, Japan
[b]Graduate School of Chemical Sciences and Engineering, Hokkaido University, Sapporo 060-8628, Japan

†Electronic supplementary information (ESI) available: Synthesis, Schemes S1-S3, Fig. S1-S9, Grazing incidence X-ray scattering (GIXS) data analysis, Fig. S10, Table S1, Fig. S2. See DOI: 10.1039/

ABSTRACT: The nanoscale film morphologies of three-armed cage block copolymers in three different variations (*Cage*-A, -B, and -C) have been investigated for the first time *via* synchrotron grazing incidence X-ray scattering. For all cage block copolymers, the individual block components revealed amorphous characteristic. Nevertheless, they all exhibited either cylindrical or lamellar phase-separated nanostructures. Key structural parameters such domain spacing (*d*-spacing), structural ordering, and orientation were varied depending on the cage topologies. In particular, the *d*-spacing of nanostructures ranged in 6.50–10.85 nm. Compared to their linear block copolymer analogue, the cage block copolymers achieved 54.8–74.5% *d*-spacing reduction. Overall, structural parameters such as *d*-spacing, structural ordering, and orientation were found to be correlated to the topological confinement which originate from the molecular cage topology.

Keywords: cage topology, synchrotron grazing incidence X-ray scattering, nanoscale film morphologies, structural parameters, domain spacing, structural orientation, topological confinement effect

INTRODUCTION

Synthetic cyclic polymers were first introduced in 1940s as a new interesting polymer family[1-3] and then found to exhibit unique topological effects in properties due to the molecular geometry and the absence of chain ends.[4] Immediately, the synthesis of new cyclic polymers and their derivatives has been challenged in the polymer community. As a result of research progress, several synthetic methods have been developed, producing various topological cyclic polymers.[5-18] The development effort has been focused mainly for producing polymers as a single macrocycle.[5-14] In contrast, polymers possessing cage topology, a complex variant of cyclic topology, have been reported in a limited basis because of difficulties of the synthesis.[10-12,15-19] Despite the difficulties, a few cage homopolymers and block copolymers have been prepared successfully: polytrahydrofurans,[18-22] polystyrenes,[23-25] poly(ε-caprolactone)s,[26-28] poly(ethylene oxide),[29] and poly(*n*-decyl glycidyl ether) and poly(2-(2-(2-methoxyethoxy)ethoxy)ethyl glycidyl ether) blocks.[30] Cage topology could be interpreted as a complex variant of cyclic topology, which suggests similar topological influences on polymer morphology such as domain spacing reduction could be expected. As a matter of fact, it has been demonstrated that the compact chain conformation brought by cage topology reduces the overall domain spacing of self-assembled lamellar nanostructures of poly(ε-caprolactone)s.[27,28] Nevertheless, the reports are only based on poly(ε-caprolactone)s, and morphologies and properties of other homopolymer cages and especially those based on block copolymers are relatively less explored than the synthetic reports.

In this study, we report the first nanoscale film morphologies of various three-armed cage block copolymers composed of poly(*n*-decyl glycidyl ether) (PDGE) and poly(2-(2-(2-methoxyethoxy)ethoxy)ethyl glycidyl ether) (PTEGGE) in near equivalent volume fractions. Synchrotron grazing incidence X-ray scattering (GIXS) analysis found the cage block copolymers, namely *Cage*-A, *Cage*-B, and *Cage*-C, formed phase-separated nanostructures in films. Interestingly,

all copolymers revealed either cylindrical or lamellar nanostructures depending on their molecular topologies. Excitingly, they all produce significantly reduced domain spacings, which could not be achievable from the linear block copolymer counterpart. The degree of domain spacing reduction is dependent upon the cage topologies. The structural parameters are varied further with the molecular topologies.

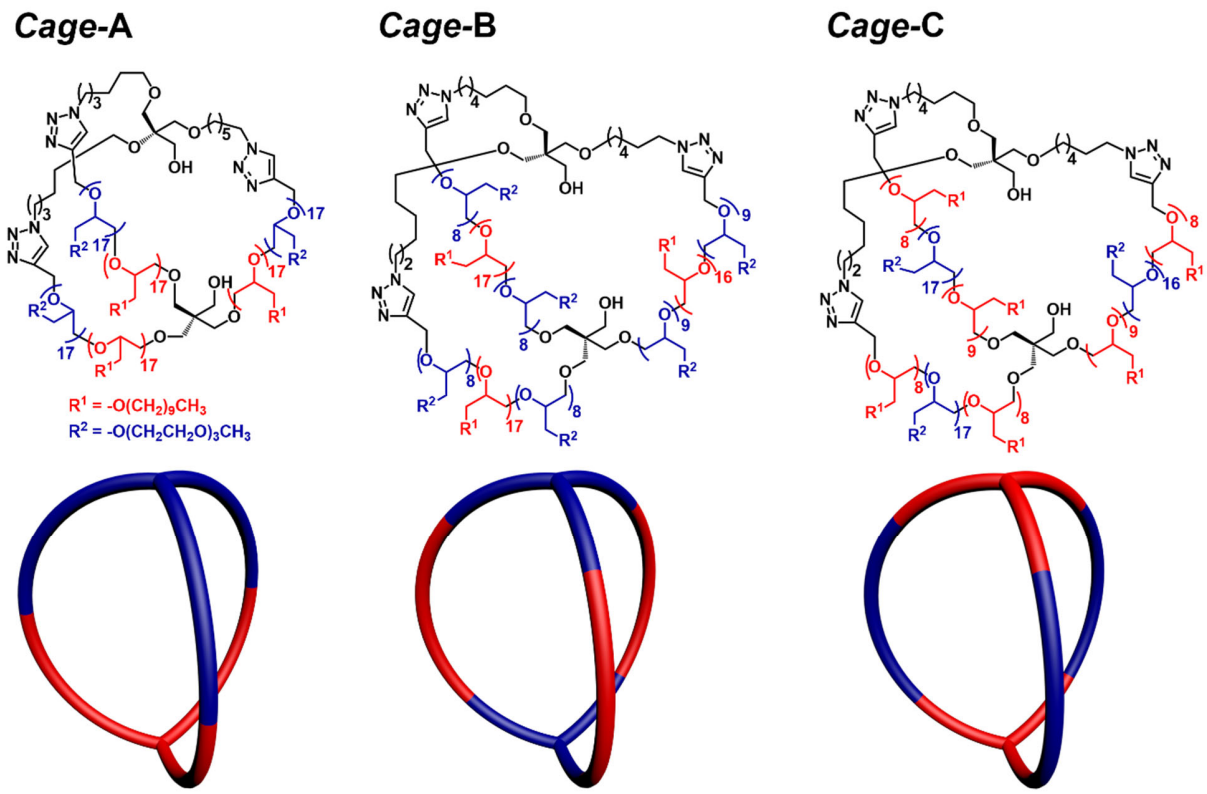

Fig. 1 Chemical structures of cage block copolymers with various molecular topologies.

Table 1. Molecular characteristics of various cage block copolymers and their homopolymers [a]

Polymer	$M_{n,NMR}$ [b] (g mol^{-1})	$Đ$ [c]	ρ_e [d] (nm^{-3})	ρ_m [e] (g cm^{-3})	PDGE block		PTEGGE block	
					DP_{PDGE} [f]	ϕ_{PDGE} [g]	DP_{PTEGGE} [h]	ϕ_{PTEGGE} [i]
Cage-A	22,600	1.02			49	0.494	51	0.506 [j]
Cage-B	22,600	1.02			50	0.504	50	0.496
Cage-C	22,600	1.03			50	0.504	50	0.496
c-PDGE [k]	11,000	1.02	310	0.92				
l-PDGE [l]	11,100	1.03	341	1.01				
l-PTEGGE [m]	11,200	1.04	353	1.05				

[a]Characterization data from references no. 30 and 31. [b]Number-average molecular weight of polymer determined by ^{1}H NMR spectroscopic analysis. [c]Dispersity determined by size exclusion chromatography (SEC) analysis in tetrahydrofuran. [d]Electron density of homopolymers in films determined by X-ray reflectivity analysis. [e]Mass density of homopolymers in films obtained from the electron density determined by X-ray reflectivity analysis. [f]Number-average degree of polymerization of PDGE block determined by ^{1}H NMR spectroscopic analysis. [g]Volume fraction of PDGE block estimated from the $M_{n,NMR}$ and ρ_m data. [h]Number-average degree of polymerization of PTEGGE block determined by ^{1}H NMR spectroscopic analysis. [i]Volume fraction of PTEGGE block estimated from the $M_{n,NMR}$ and ρ_m data. [j]Volume fraction estimated under the assumption that the ρ_m values of PTEGGE blocks in *Cage*-A, -B, and -C are 8.9% lower than that of the linear PTEGGE homopolymer, as observed for the linear and cyclic PDGE homopolymers; specifically, the PTEGGE blocks are assumed to have $\rho_m = 0.96$ g cm^{-3}. [k]Cyclic PDGE homopolymer. [l]Linear PDGE homopolymer. [m]Linear PTEGGE homopolymer.

Experimental

Cage-A, *Cage*-B, and *Cage*-C were synthesized according to the synthetic schemes (Scheme S1-S3 in Electronic Supplementary Information ESI†) reported previously.[30,31] The synthetic details are given in ESI† and molecular characteristics of the copolymers are summarized in Table 1. Additionally, differential scanning calorimetry (DSC) thermograms (see Fig. S10 and Table S1, ESI†) of each copolymer were measured with a ramping rate of 10 °C min^{-1} under nitrogen atmosphere (model DSC7020, Hitachi Instrument, Tokyo, Japan).

Nanoscale films of individual copolymer were prepared by spin-coating copolymer solutions onto silicon substrates. Copolymer solutions were prepared with 0.5 wt% concentration in tetrahydrofuran and filtrated through disposable syringes equipped with polytetrafluoroethylene filter membranes (0.2 μm pore size) prior to spin coating. The obtained copolymer films were then dried

in vacuum at room temperature for 24 h. The thickness of films were measured to range within 100–120 nm by using a spectroscopic ellipsometer (Model M-2000, Woollam, Lincoln, NE, USA). The films were kept at room temperature in vacuum before X-ray scattering measurements.

GIXS measurements were conducted at the 3C Beamline of the PLS-II facility in Pohang Accelerator Laboratory (PAL), Pohang, Korea.[32-34] The sample-to-detector distance (SDD) was set 214.7 mm for grazing-incidence wide-angle X-ray scattering (GIWAXS) measurements and 2951.3 mm for grazing-incidence small-angle X-ray scattering (GISAXS) measurements. The wavelength λ of incident X-ray beam was set to 0.12411 nm and the incidence angle α_i was set in the range of 0.1254–0.1850° with respect to the film plane. A two-dimensional (2D) charge-coupled detector (CCD) (model Rayonix 2D SX 165, Rayonix, Evanston, IL, USA) was used to obtain 2D scattering images; a set of aluminum foils was used as a semi-transparent beam stop. Each data was measured at room temperature, and with exposure time of 10–30 s. The scattering angles were corrected by using a precalibrated polystyrene-*block*-poly(ethylene-*random*-butylene)-*block*-polystyrene and silver behenate standards (Tokyo Chemical Inc., Tokyo, Japan); the positions of the X-ray beams reflected from the silicon substrate were used additionally.

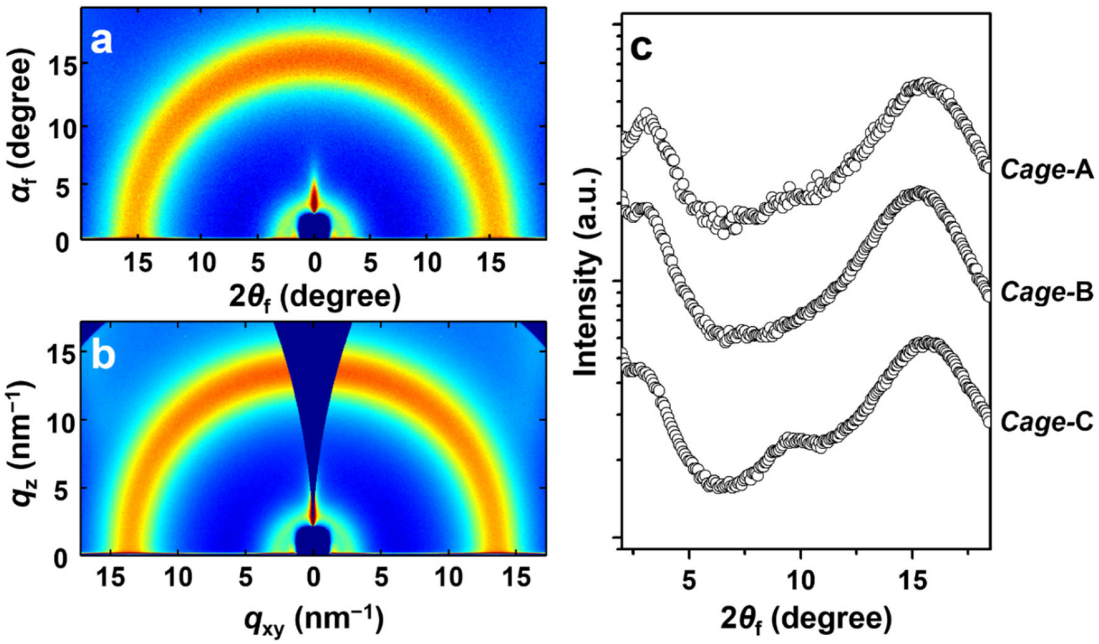

Fig. 2 Representative GIWAXS data of the nanoscale films (100–120 nm thick) of cage block copolymers measured with SDD = 214.7 mm at room temperature using a synchrotron X-ray beam (λ = 0.12411 nm): (a) 2D scattering image in angle space ($2\theta_f$ and α_f) of *Cage*-B (α_i = 0.1740°); (b) 2D scattering image in scattering vector space (q_{xy} and q_z) obtained from the scattering image in (a); (c) in-plane scattering profiles extracted along the equatorial line at chosen α_f values (0.300° for *Cage*-A, 0.279° for *Cage*-B, and 0.290° for *Cage*-C) from the measured 2D scattering images, including (a).

RESULTS AND DISCUSSION

The glass transitions and crystal melting points of cage block copolymers were confirmed to occur below −70.8 °C and 21.0 °C, respectively, according to their DSC thermograms (Fig. S1 and Table S1, ESI†). Because all phase transitions occur below 21.0 °C, the 100–120 nm block copolymer films were considered to be thermally annealed from both the drying process and the storage period prior to GISAXS and GIWAXS measurements. All scattering measurements were also performed at room temperature.

Fig. 2a is the representative 2D GIWAXS image of the *Cage*-B block copolymer, in which the two isotropic scattering peaks at approximately 3.1° and 15.6° correspond to *d*-spacing values of 2.3 nm and 0.46 nm, respectively. Due to their visual appearance, the two isotropic peaks are commonly regarded as amorphous halos. Such amorphous halos are also observed for *Cage*-A and *Cage*-C

(GIWAXS image not shown). The in-plane 1D scattering profiles extracted from the measured data are shown in Fig. 2c, in which the peaks near 3° can be assigned to the mean interdistance between the backbone chains of copolymers, and the peak near 15° corresponds to the mean intramolecular and intermolecular interdistances between *n*-decyl and 2-(2-(2-methoxyethoxy)ethoxy)ethyl bristles. Interestingly, *Cage*-C revealed an additional peak at 9.8° (*d*-spacing = 0.73 nm), which could also be assigned to the mean interdistance between the side chains and the backbone chains of copolymers. The intensity of this peak, however, is relatively weaker than the two other peaks. Overall, both PDGE and PTEGGE blocks of cage block copolymers are amorphous inside the nanoscale film.

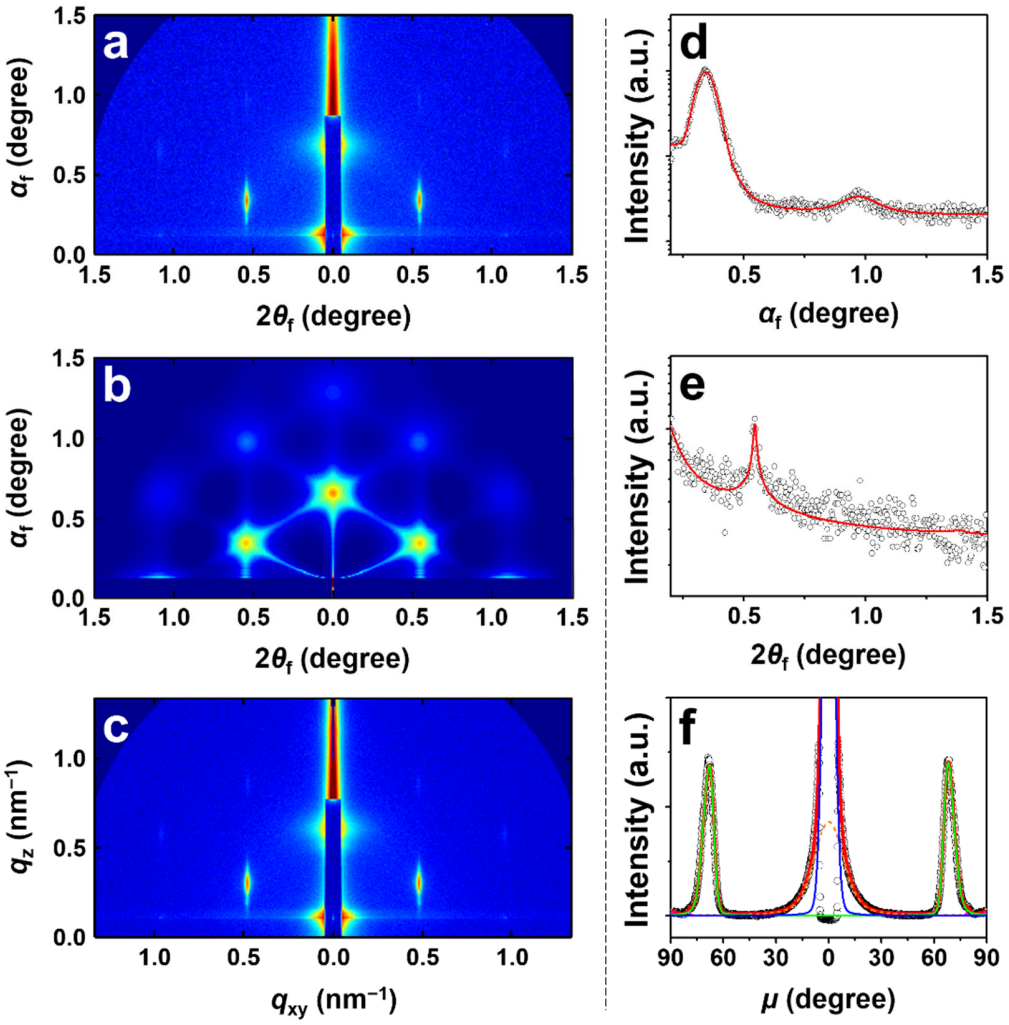

Fig. 3 Representative GISAXS data of *Cage*-A films (100–120 nm thick) measured with α_i = 0.1254°; SDD = 2951.3 mm at room temperature using a synchrotron X-ray beam (λ = 0.12411 nm): (a) 2D scattering image in angle space. (b) 2D scattering image reconstructed from the structural parameters from data analysis. (c) 2D scattering image in scattering vector space obtained from the scattering image in (a). (d) Out-of-plane scattering profile along the meridian line at $2\theta_f$ = 0.544° of image in (a). (e) In-plane scattering profile along the equatorial line at α_f = 0.182° of image in (a). In (d) and (e), open circles are the measured scattering intensities and solid red lines represent the calculated intensities based on the GIXS formula of cylindrical structure model. (f) Azimuthal scattering profile along the azimuth at q = 0.607 nm^{-1} of image in (c) where the open circles are the measured intensities and the solid lines represent the deconvolutions of the measured data: the solid blue and green lines are the scattering peaks of cylindrical domains in hexagonal packing order, the dashed magenta line is the Yoneda peak, the dashed orange line is a part of the reflected X-ray beam, and the solid red line is the sum of all deconvoluted peaks.

Fig. 3a is a representative GISAXS image produced by *Cage*-A films at room temperature, which reveals a clear hexagonal array of peaks. The relative scattering vector lengths of the peaks at α_f = 0.344° and 0.969° along the meridian line at $2\theta_f$ = 0.544° are 1 and $\sqrt{3}$, respectively, from the specular reflection. These are indications of a hexagonally packed cylindrical structure in horizontal orientation (*i.e.* parallel to the plane of film substrate). Hence, the scattering data (Fig. 3a) was quantitatively analyzed with the GIXS formula of a hexagonally packed cylinder model (details provided in Electronic Supplementary Information, ESI†) in which "core-shell" based two-phase cylinders are surrounded by a matrix phase derived for this study. The 1D out-of-plane and in-plane scattering profiles extracted along the meridian line at $2\theta_f$ = 0.544° (Fig. 3d) and the equatorial line at α_f = 0.182° (Fig. 3e), respectively, were successfully fitted with the hexagonally packed cylinder model. The structural parameters obtained from the analysis is summarized in Table 2. In addition, an azimuthal scattering profile extracted at q = 0.607 nm^{-1} from the q-space image (Fig. 3c) was analyzed successfully (Fig. 3f) and confirmed the horizontal orientation of the cylindrical structure (orientation parameters are summarized in Table 2). The confidence of data analysis was confirmed through the good agreement between the reconstructed 2D scattering image (Fig. 3b) based on the obtained structural parameters using the GIXS formula, and the measured GISAXS image. The schematic representation of the determined cylindrical structure is shown in Fig. 4a.

Table 2. Structural parameters of nanoscale morphologies of various cage block copolymers

Nanoscale Film Morphology	Cage-shaped block copolymers				
	Cage-A 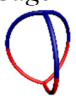	*Cage*-B 		*Cage*-C 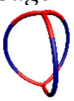	
Hexagonally packed cylinders	Horizontal				
L_z [a] (nm)	10.85				
L_y [b] (nm)	6.50				
γ [c]	1.67				
R_z [d] (nm)	5.40				
R_y [e] (nm)	2.10				
r_{cz} [f] (nm)	2.60 (0.30) [t]				
r_{cy} [g] (nm)	1.00 (0.20)				
t_{sz} [h] (nm)	2.80 (0.60)				
t_{sy} [i] (nm)	1.10 (0.30)				
ε [j]	2.57				
g [k]	0.06				
$\overline{\varphi}$ [l] (deg.)	0				
σ_φ [m] (deg.)	3.10				
O_s [n]	0.991				
ϕ [o] (vol%)	100				
Lamellae		Horizontal	Vertical	Horizontal	Vertical
D_L [p] (nm)		6.95	6.90	6.50	6.70
l_1 [q] (nm)		2.10 (0.30)	2.10 (0.30)	1.60 (0.50)	1.70 (0.30)
l_2 [r] (nm)		1.30 (0.20)	1.30 (0.20)	1.60 (0.60)	1.60 (0.50)
l_3 [s] (nm)		2.25	2.20	1.70	1.80
g		0.33	0.31	0.35	0.28
$\overline{\varphi}$ (deg.)		0	70.00	0	90
σ_φ (deg.)		18.35	16.20	6.13	27.55
O_s		0.829	-0.212	0.969	-0.221
ϕ (vol%)		34.5	65.5	33.9	66.1

[a]Mean interdistance between the arrays of cylinders in {001} plane. [b]Mean center-to-center distance of the cylindrical domains in the film plane direction. [c]Ratio between L_z and L_y (= L_z/L_y). [d]Total semi-major radius of cylinders along the *z*-axis (normal to film plane). [e]Total semi-minor radius of cylinders along the *y*-axis (parallel to film plane). [f]Semi-major radius of cylinder core along the *z*-axis. [g]Semi-minor radius of cylinder core along the *z*-axis. [h]Thickness of cylinder shell along the *z*-axis. [i]Thickness of cylinder shell along the *y*-axis. [j]Elliptical axial ratio (=R_z/R_y). [k]Lattice distortion factor of nanostructure (*i.e.*, hexagonal cylinder structure or lamellar structure). [l]Mean value of the polar angle φ (*i.e.*, orientation angle) between the orientation vector $\boldsymbol{n}$ (which is set along a direction normal to the {001} plane of cylinders or to the lamellar plane) and the out-of-plane direction of the film. [m]Standard deviation for the polar angle φ. [n]Second order orientation factor of nanostructure (*i.e.*, hexagonal cylindrical structure or lamellar structure). [o]Volume fraction in percent. [p]Long period of lamellar structure. [q]Thickness of the l_1 layer. [r]Thickness of the l_2 layer, *i.e.*, interfacial layer *i*. [s]Thickness of the l_3 layer. [t]Standard deviation.

The quantitative GISAXS analysis of Fig. 3a confirmed that a hexagonally packed cylindrical structure was formed by the phase-separation between PDGE and PTEGGE blocks of *Cage*-A. The cylinders revealed an elliptical nature, in which they are defined by a semi-major radius R_z of 5.40 nm [= 2.60 (r_{cz}, core radius) + 2.80 nm (t_{sz}, shell thickness)] and a semi-minor radius R_y of 2.10 nm [= 1.00 (r_{cy}) + 1.10 nm (t_{sy})]. R_z and R_y are in the out-of-plane direction (*i.e. z*-axis) and the in-plane direction (*i.e. y*-axis) of the film, respectively. Interestingly, the elliptical axial ratio ε of the cylinders was 2.57, indicating a large deviation from the conventional circular shape. This particular feature was paired with the nonconventional *d*-spacings of the cylinders. The cylinders revealed L_y of 6.50 nm along the film plane, L_z of 10.85 nm in the out-of-plane direction. The L_z/L_y ratio γ was 1.67, which is nearly double than that $(\sqrt{3}/2)$ of conventional HEX cylinder structures. Based on these structural parameters, the volume fractions of the cylinders and matrix were calculated to be 50.5% and 49.5%, respectively. In conjunction with the molecular volume fractions of *Cage*-A (Table 1), the cylindrical domain is assigned to PTEGGE block with the PDGE blocks forming the matrix. The lattice distortion factor *g* of the hexagonal arrangement of cylinders was 0.06. The second order orientation factor O_s was 0.994 with $\overline{\varphi}$ = 0° and a standard deviation σ_φ = 3.10° (φ is the angle between the orientation vector ***n*** set normal to the {001} plane of the horizontal hexagonal cylinders as shown in Figure S11, ESI†, and the out-of-plane direction of the film).

These results collectively show that the horizontal cylinders formed by *Cage*-A exhibit notably short *d*-spacings, a high structural ordering, and a unidirectional orientation despite the nonconventional hexagonal arrangement. In particular, when compared to its linear counterpart of the same molecular weight (*linear*-PDGE-*b*-PTEGGE),[35] *Cage*-A achieved a *d*-spacing reduction of 54.8–74.5%. Furthermore, *Cage*-A exhibited a greater degree of *d*-spacing reduction when compared to the experimental observations (5–16% reduction)[36-39] and theoretical predictions (30–37% reduction)[40-43] of conventional cyclic block copolymers from the literature. Taking into account the

topology of *Cage*-A is a complex variation of cyclic topology defined by the three-armed characteristic, the observed *d*-spacing reduction is quite straightforward since the relative chain conformation of cage topology has to be more compact than a single macrocycle given that the total molecular weight of topological polymers are identical. Ultimately, this is the first demonstration of the remarkable degree of *d*-spacing reduction achieved by a three-armed cage block copolymer.

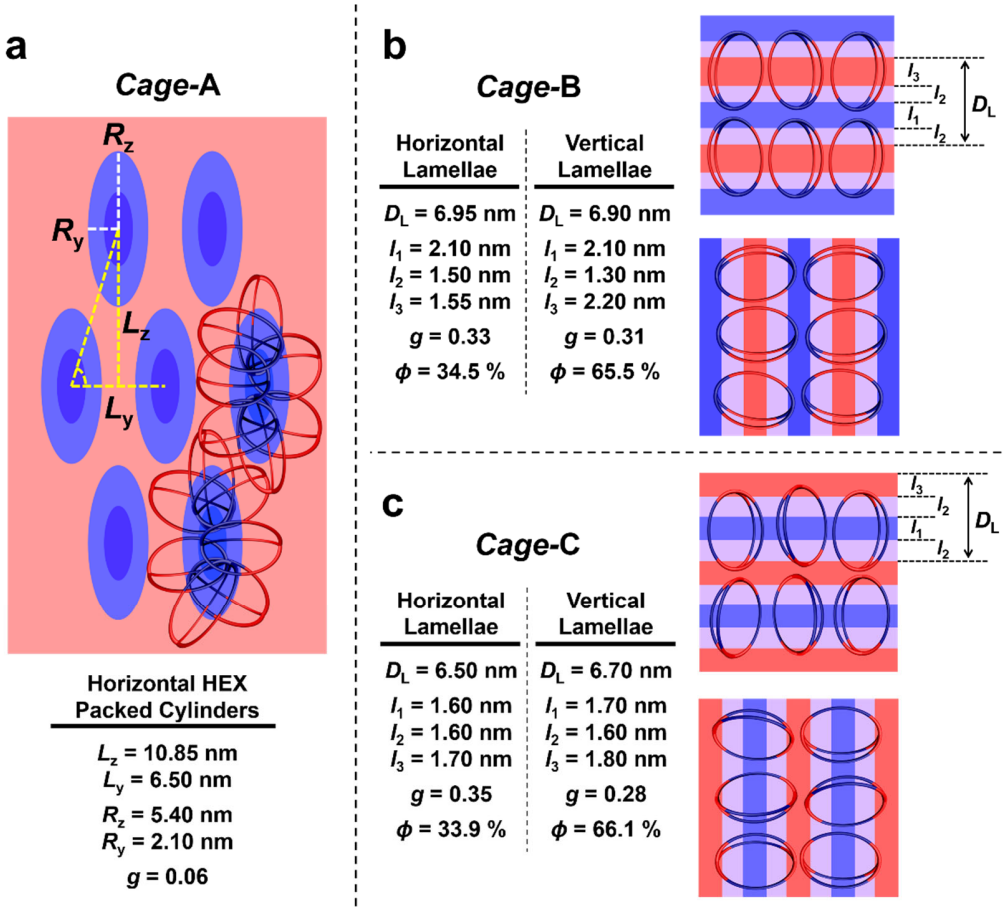

Fig. 4 Schematic representations of phase-separated nanostructures inside topological block copolymer films (cross-sectional view). (a) horizontal hexagonally-packed cylinders inside *Cage*-A film where the blue cylinder phase is assigned to PTEGGE block and the red matrix phase is assigned to PDGE block. (b) Horizontal and vertical lamellae inside *Cage*-B film where the blue sublayer is assigned to PTEGGE block and the red sublayer is assigned to PDGE block. (c) Horizontal and vertical lamellae inside *Cage*-C film where the blue sublayer is assigned to PTEGGE block and the red sublayer is assigned to PDGE block.

Cage-B films produced a GISAXS image in Fig. 5a where a scattering peak in the form of halo was observed, unlike *Cage*-A. The halo was defined by reflection positions at $\alpha_f = 0.926°$ along the

meridian line, and at $2\theta_f = 0.989°$ along the equatorial line. This is indicative of a mixture of horizontal and vertical lamellae in the film with high degrees of lamellar orientation distribution. Therefore, the scattering pattern was quantitatively analyzed where the 1D out-of-plane and in-plane scattering profiles extracted along the meridian line at $2\theta_f = 0.087°$ (Fig. 5d) and the equatorial line at $\alpha_f = 0.210°$ (Fig. 5e), respectively, were successfully fitted with the GIXS formula derived for lamellar structure model (the formula is given in ESI†). Lamellar orientations of both horizontal and vertical lamellae were evaluated from an azimuthal scattering profile extracted at q = 0.843 nm^{-1} from the q-space conversion of the raw data (Fig. 5c) to accommodate the entire scattering halo. The quantitative fitting is shown in Fig. 5f. The reconstructed 2D scattering image (Fig. 5b) confirmed the confidence of data analysis by showing good agreement with the measured GISAXS image. All structural parameters are summarized in Table 2.

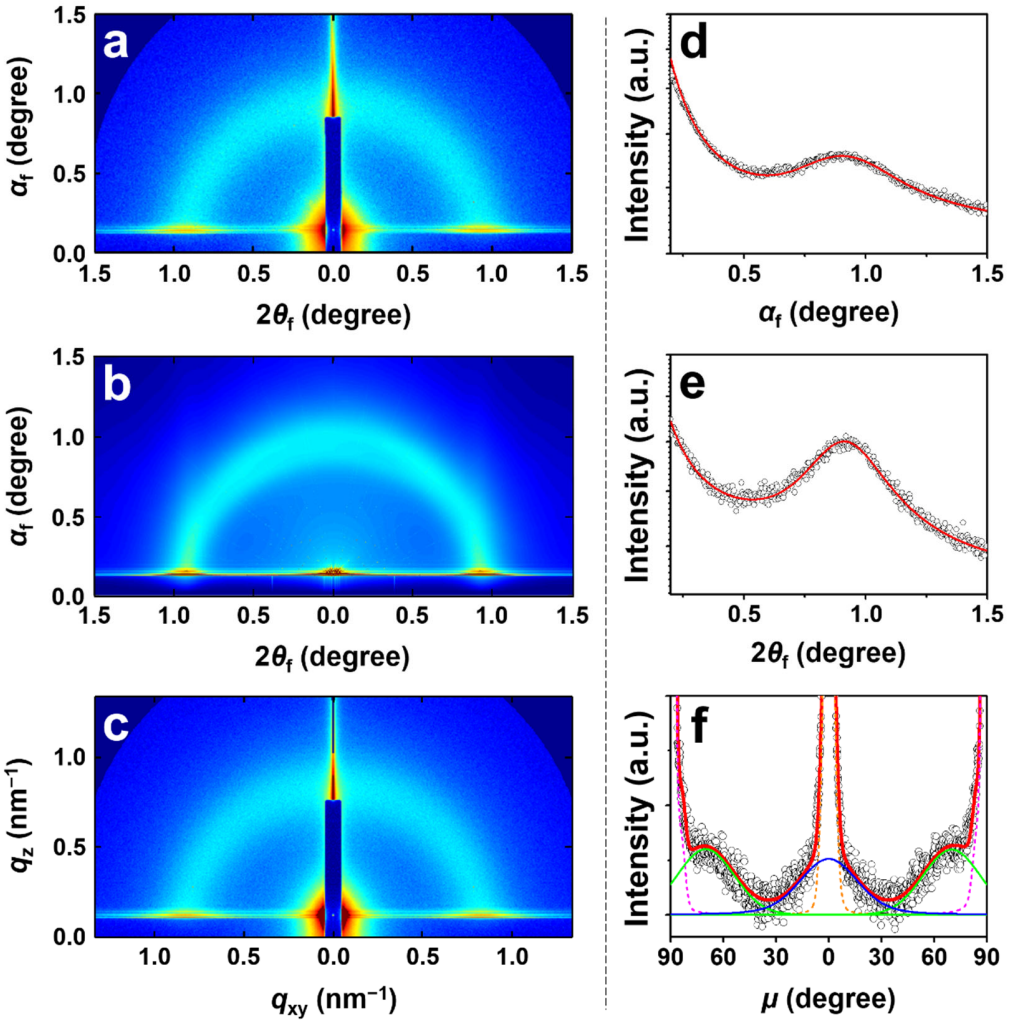

Fig. 5 Representative GISAXS data of *Cage*-B films (100–120 nm thick) measured with α_i = 0.1438°; SDD = 2951.3 mm at room temperature using a synchrotron X-ray beam (λ = 0.12411 nm): (a) 2D scattering image in angle space. (b) 2D scattering image reconstructed from the structural parameters from data analysis. (c) 2D scattering image in scattering vector space obtained from the scattering image in (a). (d) Out-of-plane scattering profile along the meridian line at $2\theta_f$ = 0.087° of image in (a). (e) In-plane scattering profile along the equatorial line at α_f = 0.210° of image in (a). In (d) and (e), open circles are the measured scattering intensities and solid red lines represent the calculated intensities based on the GIXS formula of lamellar structure model. (f) Azimuthal scattering profile along the azimuth at q = 0.843 nm^{-1} of image in (c) where the open circles are the measured intensities and the solid lines represent the deconvolutions of the measured data: the solid blue line is the scattering peak of lamellar structure, the dashed magenta line is the Yoneda peak, the dashed orange line is a part of the reflected X-ray beam, and the solid red line is the sum of all deconvoluted peaks.

The quantitative GISAXS analysis of Fig. 5a confirmed horizontal and vertical lamellae are formed in the film with volume fractions of 34.5 and 65.5 %, respectively. The horizontal lamellae are defined by a long period D_L of 6.95 nm, in which a single lamella stack consist of sublayers l_1

(2.10 nm), l_2 (1.30 nm), and l_3 (2.25 nm). The vertical lamellae exhibit similar structural parameters. Taking into account the molecular volume fraction of *Cage*-B (Table 1), the l_1 and l_3 sublayers are assigned to PTEGGE and PDGE blocks, respectively; the l_2 sublayer is the interfacial layer l_i between the PTEGGE and PDGE sublayers. Both *g* factor and σ_φ are slightly smaller for the vertical lamellae, compared to the horizontal lamellae. These results suggest that the vertical lamellar structure exhibits a slightly higher structural integrity as well as a better orientation control than the horizontal lamellae. The schematic representation of the determined lamellar structures are shown in Fig. 4b.

Overall, the morphological behavior of *Cage*-B was different from *Cage*-A given the lamellar structure and the shorter *d*-spacing. Also, its overall structural integrity was lower, suggesting an observation where the shorter *d*-spacing seems to be achieved at the cost of sacrificing structural order ($g_{Cage\text{-A}} = 0.06$; $g_{Cage\text{-B}} = 0.31, 0.31$). Comparing the PDGE/PTEGGE block arrangement within the cage topology for the two copolymers, *Cage*-B and -A resemble that of triblock and diblock copolymer, respectively. Hence, the particular block arrangement of *Cage*-B is the enabling factor of the shorter *d*-spacing. Interestingly, *Cage*-B formed a lamellar structure unlike that of *Cage*-A, indicating that the block arrangement seems to play the critical role in shifting the phase diagram for the cage block copolymers.

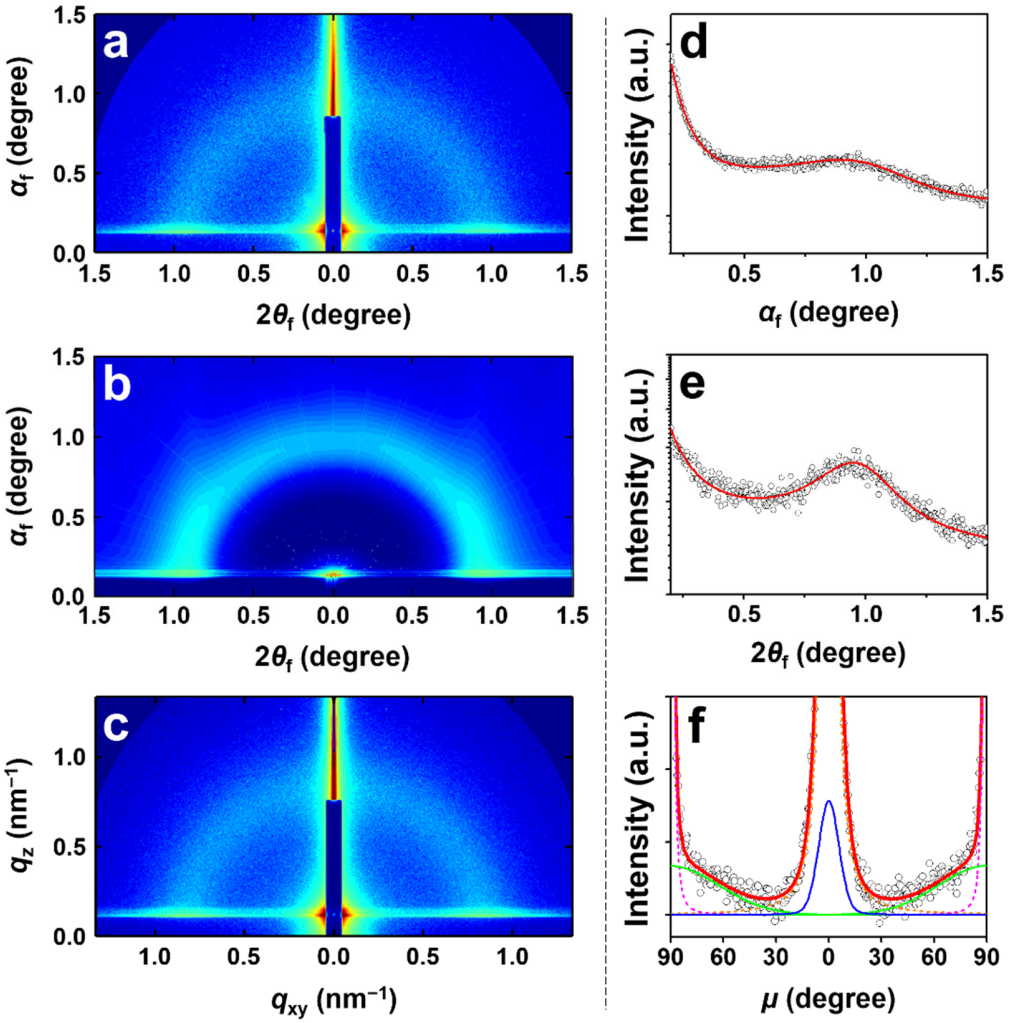

Fig. 6 Representative GISAXS data of *Cage*-C films (100–120 nm thick) measured with α_i = 0.1392°; SDD = 2951.3 mm at room temperature using a synchrotron X-ray beam (λ = 0.12411 nm): (a) 2D scattering image in angle space. (b) 2D scattering image reconstructed from the structural parameters from data analysis. (c) 2D scattering image in scattering vector space obtained from the scattering image in (a). (d) Out-of-plane scattering profile along the meridian line at $2\theta_f$ = 0.071° of image in (a). (e) In-plane scattering profile along the equatorial line at α_f = 0.199° of image in (a). In (d) and (e), open circles are the measured scattering intensities and solid red lines represent the calculated intensities based on the GIXS formula of lamellar structure model. (f) Azimuthal scattering profile along the azimuth at q = 0.827 nm^{-1} of image in (c) where the open circles are the measured intensities and the solid lines represent the deconvolutions of the measured data: the solid blue line is the scattering peak of lamellar structure, the dashed magenta line is the Yoneda peak, the dashed orange line is a part of the reflected X-ray beam, and the solid red line is the sum of all deconvoluted peaks.

The GISAXS image of *Cage*-C films strongly resembled that of *Cage*-B as shown in Fig. 6a with a scattering halo. Similar to *Cage*-B, *Cage*-C formed a mixture of horizontal and vertical lamellae with high degrees of lamellar orientation distribution. Therefore, the scattering pattern was

quantitatively analyzed where the 1D out-of-plane and in-plane scattering profiles extracted along the meridian line at $2\theta_f = 0.071°$ (Fig. 6d) and the equatorial line at $\alpha_f = 0.200°$ (Fig. 6e), respectively, were successfully fitted with the GIXS formula for lamellar structure model. The reconstructed 2D scattering image (Fig. 6b) confirmed the confidence of data analysis by showing good agreement with the measured GISAXS image. The azimuthal scattering profile extracted at $q = 0.977$ nm^{-1} from Fig. 6c was quantitatively analyzed (Fig. 6f) to evaluate the lamellar orientations. All structural parameters are summarized in Table 2.

Similar to Cage-*B*, the quantitative GISAXS analysis of Fig. 6a confirmed horizontal and vertical lamellae are formed in the *Cage*-C film with volume fractions of 33.9 and 66.1%, respectively. The horizontal lamellae are defined by the following structural parameters: $D_L = 6.50$ nm, $l_1 = 1.60$ nm, $l_2 = 1.60$ nm, $l_3 = 1.70$ nm, $g = 0.35$, and $\sigma_\varphi = 6.13$. Similar structural parameters are determined for the vertical lamellae. However, the vertical lamellae exhibit slightly smaller g factor but much larger σ_φ value, compared to those of the horizontal lamellae. Taking into consideration the molecular volume fractions of PDGE and PTEGGE blocks, the l_1 and l_3 sublayers can be assigned by the PTEGGE and PDGE block phases respectively. The schematic representation of the determined lamellar structures are shown in Fig. 4c. The block arrangement of *Cage*-C is the opposite of *Cage*-B, which immediately explains the similar structural parameters between the two copolymers. There are some notable subtle differences between the pair, however, such as the slightly shorter *d*-spacing of *Cage*-C lamellae than *Cage*-B lamellae. Also, the horizontal lamellae of *Cage*-C exhibited a higher degree of orientation control than that of *Cage*-B ($O_{s,Cage\text{-}C,hor} = 0.969$, $O_{s,Cage\text{-}B,hor} = 0.829$; see Table 2). This brings the discussion to the differences in the block arrangement between *Cage*-A versus *Cage*-B and -C.

Considering the similar degrees of polymerization and volume fractions for PDGE and PTEGGE blocks, the apparent differences in the morphological features between *Cage*-A versus

Cage-B and -C are due to their block arrangement within the three-armed cage topology. First of all, *Cage*-A forms a cylindrical structure whereas *Cage*-B and -C form lamellar structures. Taking into account of the typical behavior of a diblock copolymer with near equivalent volume fractions of its blocks forming a lamellar structure, this indicates that the phase diagram for *Cage*-A has shifted to favor cylinder formation as a consequence of its particular arrangement of its blocks within the cage topology. This is highly noteworthy as PDGE and PTEGGE blocks are separated in an equatorial division for *Cage*-A, which could be considered to roughly resemble that of a conventional diblock copolymer. This unique behavior may be originating from the fact that the two trios of chain ends of PDGE and PTEGGE blocks are conjoined at two molecular joints. This aspect creates a topological confinement effect where the chain conformation of PDGE and PTEGGE blocks is heavily limited. The extent of topological confinement experienced by the two blocks would differ since the *n*-decyl bristles of PDGE, which are saturated hydrocarbons with a sufficient length, is likely to induce a relatively greater stiffness (*i.e.* a longer persistence length) than PTEGGE defined by the flexible 2-(2-(2-methoxyethoxy)ethoxy)ethyl bristles. Therefore, the difference in persistence lengths of the two blocks would generate a certain degree of interfacial curvature[44,45] biased to PTEGGE domain. Given this correlation between the cage topology and the relative stiffness difference between PDGE and PTEGGE, *Cage*-A is theorized to conform to a distorted cylindrical nanostructure rather than a lamellar structure.

In contrast, the lamellar structures were formed by *Cage*-B and -C, which is quite interesting as their block arrangements roughly resemble that of a triblock copolymer. The implication of topological confinement in these two copolymers are drastically different from *Cage*-A largely due to the short chain length of the block bound to the molecular joints. In *Cage*-B, PDGE blocks have roughly 17 repeating units whereas PTEGGE blocks, which are bound to the molecular joints, consist approximately 8 repeating units. The opposite is the case for *Cage*-C. Thusly, the PDGE or PTEGGE

blocks bound to the molecular joints do not possess sufficient lengths for topological confinement to shift the phase diagram, thereby favoring lamellar formation for both *Cage*-B and -C. A different set of consequence arises from this particular form of topological confinement, however, as the structural integrity of the resulting lamellar structures are hampered greatly. This is evidenced by the high magnitude of *g*-factors denoting low lamellar ordering, as well as high σ_φ values and scattering halos indicating low control over the lamellar orientation. Hence, the highly restrictive chain conformations of either PDGE or PTEGGE blocks bound to the molecular joints cause structural defects in the lamellar structures, despite achieving sub-10 nm *d*-spacing. All discussion regarding the topological confinement, however, is formulated on the results of GISAXS characterization, and additional investigations from theoretical and different experimental methods are necessary in order to determine the extent of thermodynamic aspects of complex three-armed cage topology.

CONCLUSIONS

In this study, we have investigated the nanoscale film morphology details of three variations of three-armed cage block copolymers: *Cage*-A, -B, and -C. The synchrotron GIWAXS analysis confirmed that for all cage copolymers, the PDGE and PTEGGE blocks are amorphous at room temperature, exhibiting no crystalline characteristics. However, the GISAXS analysis found that all cage copolymers form nanostructures as a result of phase-separation of their blocks. They exhibited different types of nanostructures depending on the cage topologies. *Cage*-A formed horizontal hexagonally packed cylinders, whereas *Cage*-B and -C revealed horizontal lamellae. The *d*-spacing of nanostructures, as well as the structural ordering and orientation varies among the three cage topologies. The *d*-spacing is in the decreasing order: *Cage*-A $\gg$ *Cage*-B ~ *Cage*-C. Both the structural ordering and orientation are in the increasing order: *Cage*-B ~ *Cage*-C $\ll$ *Cage*-A. In particular, the achieved *d*-spacings range from 6.50 to 10.85 nm depending on the cage topologies,

which is quite notable considering the molecular weight of all copolymers are approximately 23,000 g mol^{-1}. Compared to the nanoscale film morphology of their linear counterpart, the cage block copolymers achieved *d*-spacing reduction of 54.8−74.5%. Moreover, the *Cage*-B and -C proved to be more efficient in reducing *d*-spacing whereas *Cage*-A exhibited superior structural ordering and orientation, thereby demonstrating the complex correlation between nanoscale film morphology and topological confinement effect.

Conflicts of Interest

The authors declare no conflict of interest.

Acknowledgements

This study was supported from JSPS Grant-in-Aid for Scientific Research (A and B) (19H00905 and 19H02769, T.S.), JSPS Grant-in-Aid for Challenging Exploratory Research (19K22209, T.S.), JST CREST (JPMJCR19T4, T.S.), the Photoexcitonix Project (Hokkaido University, T.S.), Creative Research Institute (CRIS, Hokkaido University, T. S.) and the Frontier Chemistry Center (Hokkaido University, T.S., T.I., and B.J.R.). B.J.R. was funded by the JSPS Fellowship for Young Scientists. The authors thank the Pohang Accelerator Laboratory for providing opportunities to conduct synchrotron X-ray scattering measurements.

REFERENCES

1. W. Patnode, D. F. Wilcock, *J. Am. Chem. Soc.*1946, **68**, 358−363.
2. M. J. Hunter, J. F. Hyde, E. L. Warrick, H. J. Fletcher, *J. Am. Chem. Soc.*1946, **68**, 667−672.
3. D. W. Scott, *J. Am. Chem. Soc.* 1946, **68**, 2294−2298.
4. B. H. Zimm, W. H. Stockmayer, *J. Chem. Phys*. 1949, **17**, 1301−1314.
5. J. A. Semlyen, Cyclic Polymers, 2nd ed., Kluwer Academic Publishers: Dordrecht, Netherlands, 2002.
6. K. Endo, *Adv. Polym. Sci.* 2008, **217**, 121−183.
7. B. A. Laurent, S. M. Grayson, *Chem. Soc. Rev.* 2009, **38**, 2202–2213.
8. H. R. Kricheldorf, *J. Polym. Sci. Part A: Polym. Chem.* 2010, **48**, 251− 284.

9. D. E. Lonsdale, M. J. Monteiro, *J. Polym. Sci. Part A: Polym. Chem.* 2011, **49**, 4603–4612.
10. Z. Jia, M. J. Monteiro, *J. Polym. Sci. Part A: Polym. Chem*. 2012, **50**, 2085−2097.
11. Z. Jia, M. J. Monteiro, *Adv. Polym. Sci.* 2013, **262**, 295−328.
12. Y. Tezuka, Ed., Topological Polymer Chemistry: Progress of Cyclic Polymers in Syntheses, Properties and Functions, World Scientific: Singapore, 2013.
13. H. Wang, L. Zhang, B. Liu, B. Han, Z. Duan, C. Qi, D. Park, I. Kim, *Macromol. Rapid Commun*. 2015, **36**, 1646−1650.
14. L. Xiang, W. Ryu, H. Kim, M. Ree, *Polymers* 2018, **10**, 577.
15. T. Isono, Y. Satoh, K. Miyachi, Y. Chen, S.-i. Sato, K. Tajima, T. Satoh, T. Kakuchi, *Macromolecues* 2014, **47**, 2853−2863.
16. Z. Zhao, Q. Zhu, Z. Wang, J. Lu, Z. Jin, H. Liu, *Macromolecules* 2017, **50**, 8907−8915.
17. T. Isono, T. Sasamori, K. Honda, Y. Mato, T. Yamamoto, K. Tajima, T. Satoh, *Macromolecules* 2018, **51**, 3855–3864.
18. Y. Tezuka, *Polym. J.* 2012, **44**, 1159–1169.
19. Y. Tezuka, A. Tsuchitani, Y. Yoshioka, H. Oike, *Macromolecules* 2003, **36**, 65–70.
20. M. Igari, H. Heguri, T. Yamamoto, Y. Tezuka, *Macromolecules* 2013, **46**, 7303−7315.
21. Y. Tezuka, K. Fujiyama, *J. Am. Chem. Soc.* 2005, **127**, 6266–6270.
22. K. Kyoda, T. Yamamoto, Y. Tezuka, *J. Am. Chem. Soc.* 2019, **141**, 7526−7536.
23. J. Jeong, K. Kim, R. Lee, S. Lee, H. Kim, H. Jung, M. A. Kadir, Y. Jang, H. B. Jeon, K. Matyjaszewski, T. Chang, H. J. Paik, *Macromolecules* 2014, **47**, 3791–3796.
24. J. Zhao, Y. Zhou, Y. Li, X. Pan, W. Zhang, N. Zhou, K. Zhang, Z. Zhang, X. Zhu, *Polym. Chem.* 2015, **6**, 2879−2891.
25. A. K. Mohanty, J. Ye, J. Ahn, T. Yun, T. Lee, K.-s. Kim, H. B. Jeon, T. Chang, H.-j. Paik, *Macromolecules* 2018, **51**, 5313-5322.
26. Y. Mato, K. Honda, K. Tajima, T. Yamamoto, T. Isono, T. Satoh, *Chem. Sci.* 2019, **10**, 440–446.
27. M. Gautheir-Jaques and P. Theato, *ACS Macro Lett.*, 2020, **9**, 700−705.
28. B. J. Ree, Y. Mato, L. Xiang, J. Kim, T. Isono, T. Satoh, *Polymer Chemistry* **2021**, 12,744–758.
29. T. Noda, Y. Doi, Y. Ohta, S.-i. Takata, A. Takano and Y. Matsushita, *J. Polym. Sci.*, 2020, **58**, 2098−2107.
30. Y. Satoh, H. Matsuno, T. Yamamoto, K. Tajima, T. Isono, T. Satoh, *Macromolecules* 2017, **50**, 97−106.

31. Ree, B. J.; Satoh, Y.; Jin, K. S.; Isono, T.; Kim, W. J.; Kakuchi, T.; Satoh, T.; Ree, M. Well-Defined Stable Nanomicelles Self-Assembled by Brush Cyclic and Tadpole Copolymer Amphiphiles: A Versatile Smart Carrier Platform. *NPG Asia Materials* **2017**, *9*, e453.
32. Y. Y. Kim, B. J. Ree, M. Kido, Y.-G. Ko, R. Ishige, T. Hirai, D. Wi, J. Kim, W. J. Kim, A. Takahara, M. Ree, *Adv. Electronic Mater.* 2015, **1**, 1500197.
33. B. J. Ree, D. Aoki, J. Kim, T. Satoh, T. Takata, M. Ree, *Macromolecules* 2019, **52**, 5325−5336.
34. B. J. Ree, D. Aoki, J. Kim, T. Satoh, T. Takata, M. Ree, *Macromol. Rapid Commun*. 2019, **40**, 1900334.
35. B. J. Ree, Y. Satoh, T. Isono, T. Satoh, *Nano Lett.* 2020, **9**, 6520**–6525.**
36. S. Honda, T. Yamamoto, Y. Tezuka, *J. Am. Chem. Soc.* 2010, **132**, 10251–10253.
37. Y. Q. Zhu, S. P. Gido, H. Iatrou, N. Hadjichristidis, J. W. Mays, *Macromolecules* 2003, **36**, 148−152.
38. A. Takano, O. Kadoi, K. Hirahara, S. Kawahara, Y. Isono, J. Suzuki, Y. Matsushita, *Macromolecules* 2003, **36**, 3045−3050.
39. J. E. Poelma, K. Ono, D. Miyajima, T. Aida, K. Satoh, C. J. Hawker, *ACS Nano* 2012, **6**, 10845−10854.
40. R. L. Lescanec, D. A. Hajduk, G. Y. Kim, Y. Gan, R. Yin, S. M. Gruner, T. E. Hogen-Esch, E. L. Thomas, *Macromolecules* 1995, **28**, 3485−3489.
41. J. F. Marko, *Macromolecules* 1993, **26**, 1442−1444.
42. W. H. Jo, S. S. Jang, *J. Chem. Phys.* 1999, **111**, 1712−1720.
43. G. Zhang, Z. Fan, Y. Yang, F. Qiu, *J. Chem. Phys.* 2011, **135**, 174902.
44. M. W. Bates, S. M. Barbon, A. E. Levi, R. M. Lewis, III, H. K. Beech, K. M. Vonk, C. Zhang, G. H. Fredrickson, C. J. Hawker, C. M. Bates, *ACS Macro Lett.* 2020, **9**, 396−403.
45. A. B. Chang, F. S. Bates, *ACS Nano* 2020, **14**, 11463−11472.